NANO EXPRESS   **Open Access**

CrossMark

Preparation and Photocatalytic Performance of Hollow Structure LiNb$_3$O$_8$ Photocatalysts

Haifa Zhai[1,2*] , Jingjing Qi[1], Xiang Zhang[1], Hongjing Li[1], Liping Yang[1], Chunjie Hu[1], Hairui Liu[1] and Jien Yang[1]

Abstract

Hollow structure LiNb$_3$O$_8$ photocatalysts were prepared by a hydrothermal method assisting sintering process. The particles' aggregation to form hollow structures with obvious cavities can be attributed to the Li element volatilization during calcination process. All the LiNb$_3$O$_8$ powders show high photocatalytic efficiency of degradation of methylene blue (MB), especially for the sample calcined at 700 °C (LNO700), with only 3 h to completely decompose MB. The photo-degradation of MB follows the pseudo-first-order kinetics, and the obtained first-order rate is 0.97/h. The larger degradation rate of LNO700 can be attributed to its hollow structure which provides a larger specific surface area and more active sites to degrade the MB molecules. The cycling test of photo-degradation and adsorption of MB over LNO700 powder indicates that the hollow structure of the LiNb$_3$O$_8$ photocatalyst is stable and the LiNb$_3$O$_8$ photocatalyst is an efficient photocatalyst with good reusability, confirmed by the XRD and X-ray photoelectron spectroscopy tests before and after photo-degradation of MB.

Keywords: LiNb$_3$O$_8$, Photocatalyst, Hollow structure, Hydrothermal

Background

Recent years, energy crisis and environmental pollution have become two urgent challenges, which seriously inhibit the economic development and human health. Photocatalysis is considered as the answer to the both problems, as it has the ability to produce hydrogen and decompose organic pollutants. Since Fujishima and Honda discovered the photocatalytic splitting of water using TiO$_2$ as an electrode in 1972 [1], TiO$_2$ has been widely investigated in the degradation of organic pollutions in water. Since then, various semiconductor materials are studied to search for the most convenient photocatalyst with high efficiency, low cost, environmental friendliness, and direct utilization of sunlight.

Niobates, mainly including three groups: alkali niobates, columbite niobates, and rare-earths orthoniobates, have been widely studied in many applications such as optical devices, solid electrolytic capacitors, dye-sensitized solar cells, and catalysis due to their interesting physical and chemical properties [2–4]. For the applications of clean energy and environmental remediation, some niobates, such as BiNbO$_4$ [5, 6], LiNbO$_3$ [7], (Na, K)NbO$_3$ [8], and LiNb$_3$O$_8$ [9–15], have been investigated due to their unique distorted [NbO6] octahedral structures which provide active sites for photocatalysis. Among these materials, LiNb$_3$O$_8$ is considered as a novel lithium-ion battery (LIB) anode material with a large theoretical capacity of 389 mAh/g assuming two-electron transfers (Nb^{5+}→Nb^{3+}) [10, 11]. As a photocatalyst, LiNb$_3$O$_8$ shows efficient production of hydrogen and degradation of the organic pollutant of toluidine blue O (TBO) [12–14].

The conventional preparation method of niobates is solid-state reaction, while it always results in an inhomogeneous distribution of Li element in the preparation of Li-Nb-O compounds due to the easy volatilization of Li element at high annealing temperature. At most time, LiNb$_3$O$_8$ is easily formed and recognized as an impurity phase during the preparation of LiNbO$_3$. Compared to solid-state reaction, the hydrothermal method is widely

---

* Correspondence: haifazhai@126.com
[1]Henan Key Laboratory of Photovoltaic Materials, College of Physics and Materials Science, Henan Normal University, Xinxiang 453007, People's Republic of China
[2]National Laboratory of Solid State Microstructures, Nanjing University, Nanjing 210093, People's Republic of China

Zhai *et al. Nanoscale Research Letters* (2017) 12:519

Page 2 of 7

used to synthesize nanomaterials with a small particle size, which could provide a larger specific surface area and more active sites in the applications, especially for the photocatalytic process. Hollow structures, always accompanied with excellent performances, have attracted much attention and have been used in many fields, such as catalysis [16]. Great efforts have been made to improve the photocatalytic activity of semiconductors with various porous and hollow textures, as the hollow structure can not only lead to a higher specific area but also increase light-harvesting efficiency due to multi-scatting of light [17–23]. For a hollow structure $LiNb_3O_8$ photocatalyst, there is still no report before and the research of $LiNb_3O_8$ is still rare.

In this paper, hollow structure $LiNb_3O_8$ photocatalysts were prepared by the hydrothermal method assisting sintering process. The crystal structures, microstructures, and optical properties were studied systematically. The photocatalytic performance of hollow structure $LiNb_3O_8$ photocatalysts was evaluated by the degradation of methylene blue (MB) under UV light irradiation.

Methods
Photocatalyst Preparation
Hollow structure $LiNb_3O_8$ photocatalysts were prepared by the hydrothermal method assisting sintering process using lithium hydroxide monohydrate ($LiOH·H_2O$, Aladdin, ACS, ≥ 98.0%) and niobium pentaoxide (Nb_2O_5, Aladdin, AR, 99.9%) as raw materials without further purification. Firstly, 3.5 mmol of Nb_2O_5 was dispersed into 35 mL deionized water with a certain amount of $LiOH·H_2O$ (the mole ratio of Li:Nb = 8:1) added under magnetic stirring for 1 h. Then, the suspension solution was put into a 50-mL Teflon-lined hydrothermal synthesis autoclave reactor and maintained at 260 °C for 24 h. After cooling down to room temperature naturally, the obtained white powders were centrifuged, washed with deionized water, and dried. Finally, the powders were calcined at various temperatures from 600 to 1000 °C for 2 h with a ramp rate of 5 °C/min.

Characterization
The crystal structures of $LiNb_3O_8$ powders were analyzed using X-ray powder diffraction (XRD, Bruker D8 Discover) with Cu Kα radiation. The morphologies of the powders were characterized by field emission scanning electron microscopy (SEM, JSM-6700F) and the chemical composition was measured by energy dispersive X-ray spectroscopy (EDS) performed in SEM. The UV-vis diffuse reflectance spectra (DRS) of the powders were recorded by a UV-vis-NIR spectrophotometer (UV-3600, Shimadzu). The photoluminescence (PL) spectra were detected using a Jasco FP-6500 fluorescence spectrophotometer. The specific surface area was measured

on a surface area apparatus (Micromeritics ASAP 2460) at 77 K by N_2 adsorption/desorption method (BET method). X-ray photoelectron spectroscopy (XPS) analysis was performed on a Thermo-Fisher Escalab 250Xi instrument.

Catalytic Tests
To evaluate the photocatalytic performance of the hollow structure $LiNb_3O_8$ photocatalysts, the degradation of MB aqueous solution (10 mg/L) was carried out under irradiation of a 500-W Hg lamp at a natural pH value. Fifty milligrams of powders were dispersed into 50 mL of MB aqueous solution. Before the irradiation, the suspension was kept in the dark for 1 h under stirring to achieve adsorption equilibrium. Then, the suspension was irradiated by the Hg lamp, and the residual concentration of MB was analyzed using UV-3600 at 665 nm with an interval of 1 h. In addition, the total organic carbon (TOC) of the mixture was determined via using a high-TOC Elementar Analyzer system to investigate whether the dye is completely degraded.

To detect the active species during photocatalytic reactivity, electrons (e^-), holes (h^+), hydroxyl radicals (·OH), and the superoxide radical (O_2^-) were investigated by adding 5 mM $AgNO_3$ (a quencher of e^-), EDTA-2Na (a quencher of h^+), tert-butyl alcohol (*t*-BuOH, a quencher of ·OH), and benzoquinone (BQ, a quencher of $O_2^·$), respectively. The method was similar to the former photocatalytic activity test.

Results and Discussion
The XRD patterns of $LiNb_3O_8$ powders calcined at different temperatures for 2 h are shown in Fig. 1. As seen in the figure, at 600 °C, the main phases are $LiNbO_3$ and Nb_2O_5, no $LiNb_3O_8$ phase observed at all. At 700 °C, the
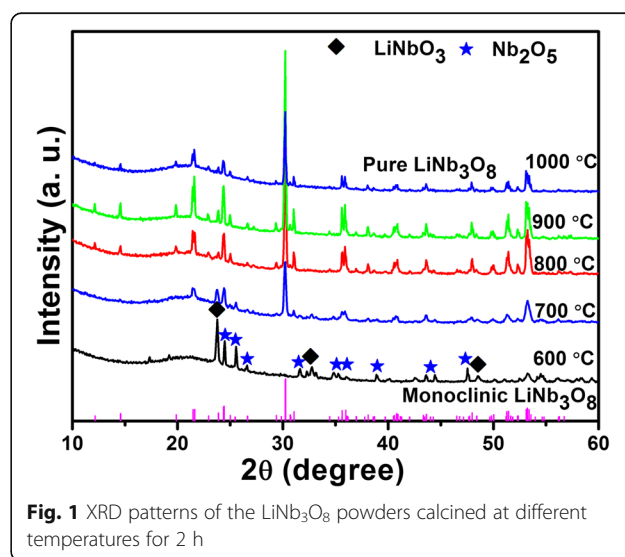
Fig. 1 XRD patterns of the $LiNb_3O_8$ powders calcined at different temperatures for 2 h

Zhai *et al. Nanoscale Research Letters* (2017) 12:519

Page 3 of 7

predominant phase is $LiNb_3O_8$, with a small amount of residual $LiNbO_3$, which means $LiNb_3O_8$ is more easily prepared by the hydrothermal method assisting sintering process than conventional methods [10, 11]. With the calcination temperature increase, only pure phase $LiNb_3O_8$ is observed and the phase is stable even up to 1000 °C; also, higher calcination temperature means better crystallinity and larger grain size. As shown in the figure, the phase is perfectly consistent with the JCPDF card no. 36-0307 (inserted in Fig. 1 as a reference), which is indexed to the monoclinic phase, a space group of P21/a.
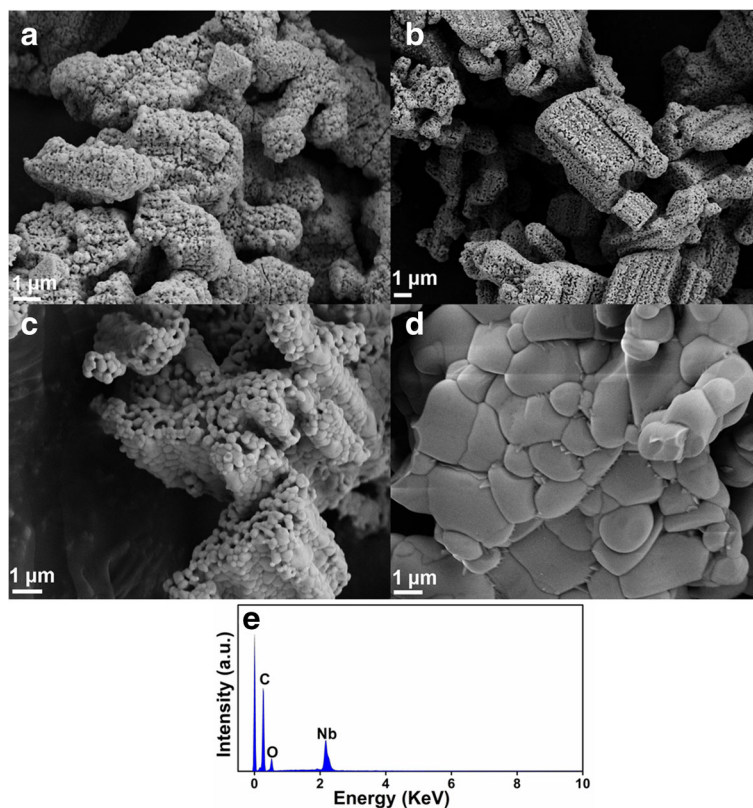
The SEM images of $LiNb_3O_8$ powders calcined at different temperatures are displayed in Fig. 2. It can be clearly seen that at 700 and 800 °C, the particles aggregate to form hollow structures with obvious cavities. It can be attributed to the Li element volatilization during calcination process, which is beneficial to the formation of new $LiNb_3O_8$ particles and networks between the particles [15]. At the same time, the connection sites and particle shapes seem indistinct in the sample at 700 °C due to its poor crystallinity. With the calcination temperature increase, the grain size increases from ~100 nm at 700 °C to 1~3 μm at 1000 °C; the particle shapes become more obvious with improved crystallinity; the cavities become less and less with the hollow structure almost disappearing at

1000 °C. As we know, a small particle size always means high specific surface area. Both high specific surface area and good crystallinity are important factors to affect photocatalytic activity, so a trade-off must be achieved [4]. The chemical composition measured by EDS is shown in Fig. 2e. It shows the presence of C, O, and Nb elements in the synthesized $LiNb_3O_8$ powders, as Li element is undetectable.

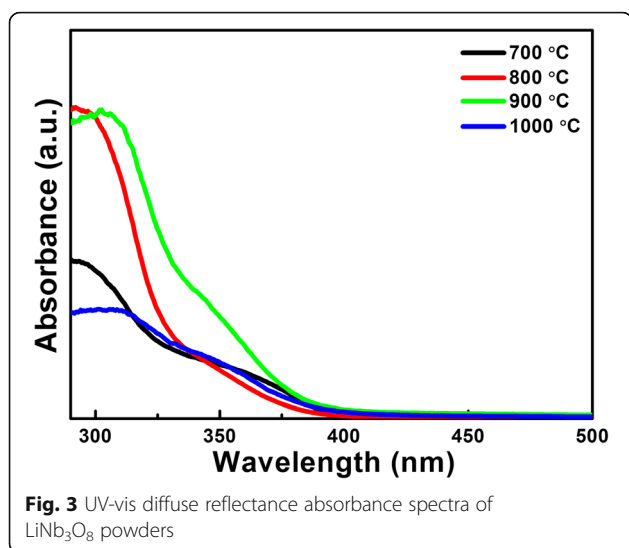The optical properties of hollow structure $LiNb_3O_8$ powders were also measured. The UV-vis diffuse reflectance absorbance spectra of $LiNb_3O_8$ powders are recorded in Fig. 3. Using a pressed $BaSO_4$ powder as the reference, the absorbance coefficient (α) is obtained from the diffuse reflectance spectra based on Kubelka-Munk (K-M) theory. As $LiNb_3O_8$ is the direct bandgap semiconductor [12], the bandgap (E_g) can be calculated according to the relation between the absorption edge and photon energy (hv) written as follows:

$$\alpha h\nu = A\left(h\nu - E_g\right)^{\frac{1}{2}} \quad (1)$$

where A is the absorbance constant of the semiconductors. The bandgaps of $LiNb_3O_8$ powders calcined at 700°, 800°, 900°, and 1000 °C (denoted as LNO700, LNO800, LNO900, and LNO1000, respectively) are estimated as

**Fig. 2** SEM images of $LiNb_3O_8$ powders calcined at **a** 700°, **b** 800°, **c** 900°, and **d** 1000 °C, respectively. **e** EDS spectrum of $LiNb_3O_8$ powders

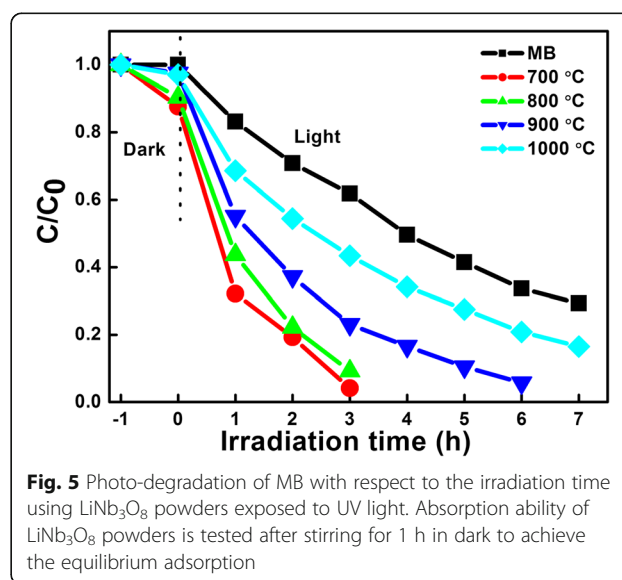Zhai *et al. Nanoscale Research Letters* (2017) 12:519

Page 4 of 7

Fig. 3 UV-vis diffuse reflectance absorbance spectra of LiNb$_3$O$_8$ powders

3.74, 3.78, 3.76, and 3.71 eV, respectively, smaller than the bandgaps reported before [12, 14]. It means the LiNb$_3$O$_8$ powders can only absorb UV light during photocatalytic process.

The separation efficiency of photogenerated carries of the LiNb$_3$O$_8$ photocatalysts is investigated by PL spectra, as shown in Fig. 4. It can be clearly seen that for the LiNb$_3$O$_8$ photocatalysts, the intensity of PL emission peak gradually weakens. As the higher PL emission peak always corresponds to the easier combination of carriers, so the LiNb$_3$O$_8$ photocatalyst exhibits better surface photogenerated electron-hole separation efficiency with the increase of calcination temperature, which can be attributed to the improved crystallinity with obvious grain size growth. Especially for LNO1000, its grain size is about several micrometers, quite different from other three hollow structure LiNb$_3$O$_8$ powders. Though higher calcination temperature which can improve the separation efficiency of photogenerated carries increases, it
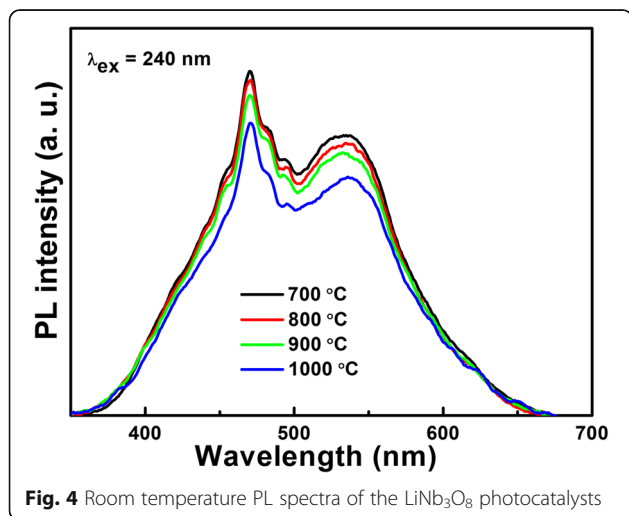
also results in the large reduce of the specific surface area, which is one of the most important factors influencing the photocatalytic efficiency. The BET areas of LNO700, LNO800, LNO900, and LNO1000 are 10.7, 4.46, 0.36, and 0.23 m^2/g, respectively; the larger surface area of LNO700 and LNO800 results from the porous and hollow structure.

The photocatalytic performance of LiNb$_3$O$_8$ powders is evaluated by the degradation of MB under UV light irradiation, as illustrated in Fig. 5. Before the irradiation, the adsorption/desorption equilibrium is achieved in the dark to investigate the adsorption ability. It shows that LNO700 and LNO800 powders show good adsorption ability, about 14 and 10%, respectively, while only 3% for both LNO900 and LNO1000; the adsorption ability is well consistent with the morphologies of the photocatalysts shown in Fig. 2. Compared with the degradation of MB without photocatalyst, all the LiNb$_3$O$_8$ powders show the higher photocatalytic efficiency of degradation of MB, especially for LNO700, with only 3 h to completely decompose MB. And the TOC% of the same sample taken after a 3-h reaction time shows 83% removal of the dye organic carbons. The difference between C/C$_0$ and TOC% value is mostly related to the presence of non-degradable intermediates. It means LiNb$_3$O$_8$ powders are efficient photocatalysts in the degradation of organic pollutants. The photocatalytic efficiency of LiNb$_3$O$_8$ catalysts is ranked in an order from the highest to the lowest: BNO700 > BNO800 > BNO900 > BNO1000. It can be seen that with the calcination temperature increases, the photocatalytic degradation ability decreases, which can be attributed to the morphologies change of LiNb$_3$O$_8$ powders: hollow structures with obvious cavities are gradually disappearing. So, hollow structures play the most important role in the degradation process, which provide a larger specific surface area and more active sites to degrade the MB


Fig. 4 Room temperature PL spectra of the LiNb$_3$O$_8$ photocatalysts

Fig. 5 Photo-degradation of MB with respect to the irradiation time using LiNb$_3$O$_8$ powders exposed to UV light. Absorption ability of LiNb$_3$O$_8$ powders is tested after stirring for 1 h in dark to achieve the equilibrium adsorption

Zhai *et al. Nanoscale Research Letters* (2017) 12:519

Page 5 of 7

molecules. For LNO700, the best photocatalytic performance may be also attributed to the synergistic effect between $LiNb_3O_8$ and $LiNbO_3$. These two niobate forms can interact with each other, and photogenerated electrons can avoid recombination more efficiently [14].

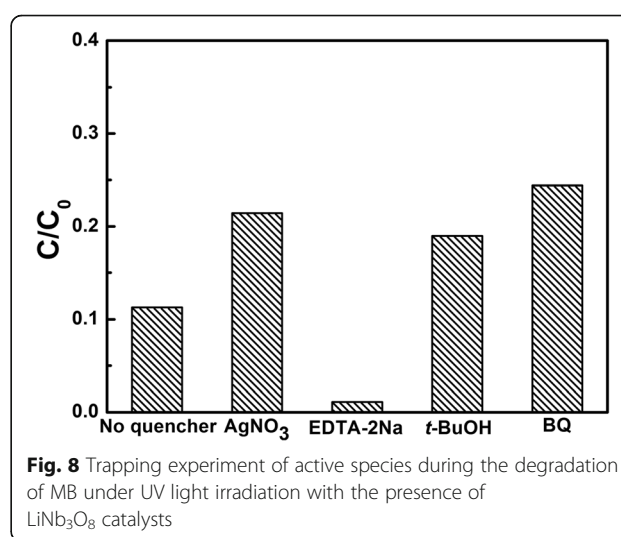The first-order rate constant (k) is also calculated to exhibit the photocatalytic ability of $LiNb_3O_8$ powders based on the modified Langmuir-Hinshelwood kinetics model [24], as shown in Fig. 6. The obtained k are 0.18, 0.97, 0.75, 0.45, and 0.25/h for MB, LNO700, LNO800, LNO900, and LNO1000, respectively. The apparent rate also shows that LNO700 with a hollow structure is the most efficient photocatalyst among them, about 4 times higher than that of LNO1000 and 5.5 times higher than that of MB without a photocatalyst.
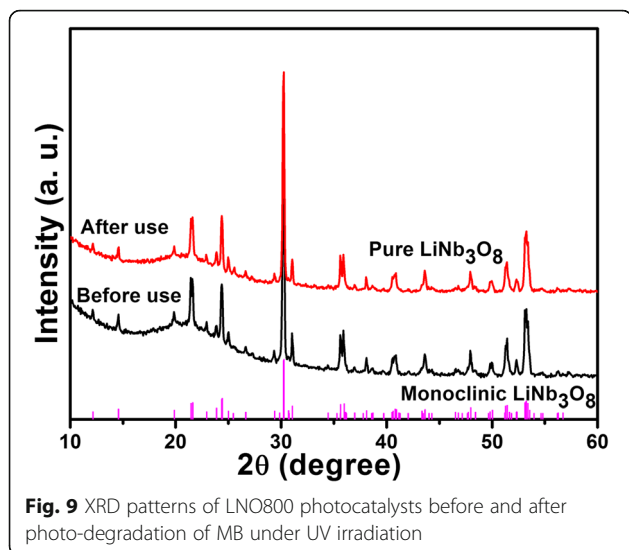
To investigate the reusability and stability of the hollow structure $LiNb_3O_8$ photocatalyst (LNO700) for both the photocatalytic degradation and adsorption ability of MB, five cycles of photo-degradation of MB are performed, as shown in Fig. 7a, b. After five cycles of photo-degradation of MB, there shows no obvious performance loss with complete decomposition of MB in 3 h. At the same time, we firstly studied the stability of the adsorption ability of LNO700, and the results show that for each cycle, the adsorption of MB under the dark can almost keep constant. It indicates that the hollow structure of the $LiNb_3O_8$ photocatalyst is stable, which guarantees that the $LiNb_3O_8$ photocatalyst with hollow structures is an efficient photocatalyst with good reusability for practical applications.

Figure 8 displays the trapping experiment of active species during the photocatalytic reaction process with LNO700 catalysts. It can be seen that the degradation of MB is obviously decreased with the addition of $AgNO_3$ (a quencher of e[−]), t-BuOH (a quencher of ·OH) and BQ (a quencher of O_2). On the contrary, the degradation increased with the addition of EDTA-2Na (a quencher of h

Fig. 7 Cycling **a** photo-degradation and **b** adsorption of MB over LNO700 powder
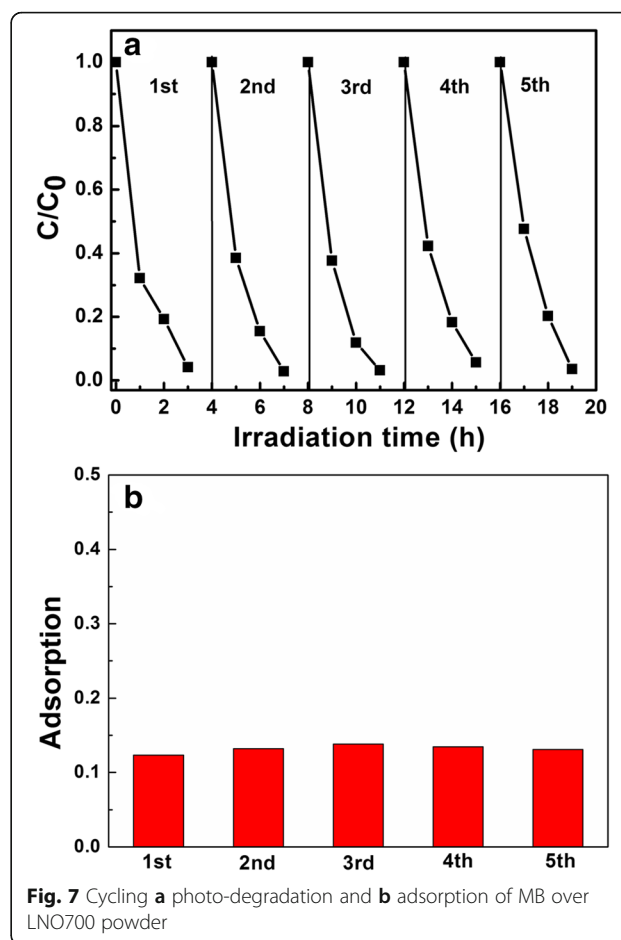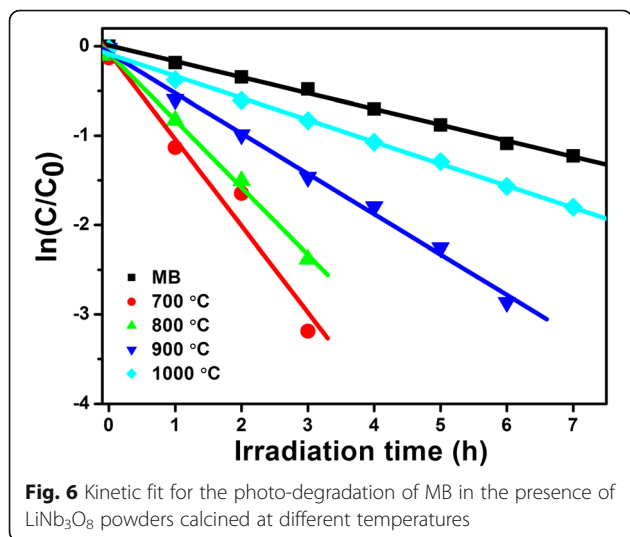
[+]), which means the separation of electrons and holes are promoted and more electrons are generated. Therefore, it can be concluded that e[−], ·OH and O_2 are the main active species in the degradation process rather than h[+]. In the photocatalytic process, the photogenerated electrons (e[−])

Fig. 6 Kinetic fit for the photo-degradation of MB in the presence of $LiNb_3O_8$ powders calcined at different temperatures

Fig. 8 Trapping experiment of active species during the degradation of MB under UV light irradiation with the presence of $LiNb_3O_8$ catalysts

Zhai *et al. Nanoscale Research Letters* (2017) 12:519

Page 6 of 7

Fig. 9 XRD patterns of LNO800 photocatalysts before and after photo-degradation of MB under UV irradiation

in the conduction band transfer to the surface of the $LiNb_3O_8$ photocatalyst and reduce molecular oxygen to superoxide anion (O_2^-); then, the superoxide anion can react with H_2O to form the active radicals (·OH) [25, 26]. These reactions would finally result in the degradation of MB.

To investigate the photocorrosion of the $LiNb_3O_8$ photocatalyst, LNO800 is characterized by XRD and XPS before and after the photo-degradation of MB, as shown in Figs. 9 and 10. The XRD results show that the crystal structures of the $LiNb_3O_8$ photocatalyst varied negligibly after use, still pure $LiNb_3O_8$ without obvious impurities. However, in the XPS spectra, Nb3d peaks are shifted to lower binding energy compared to the unused $LiNb_3O_8$, indicating that partially, Nb^{5+} has been reduced and photoreduction of $LiNb_3O_8$ occurred on the surface during the photo-degradation process [15, 27–29].

Fig. 10 XPS spectra of Nb3d for LNO800 photocatalysts before and after photo-degradation of MB under UV irradiation
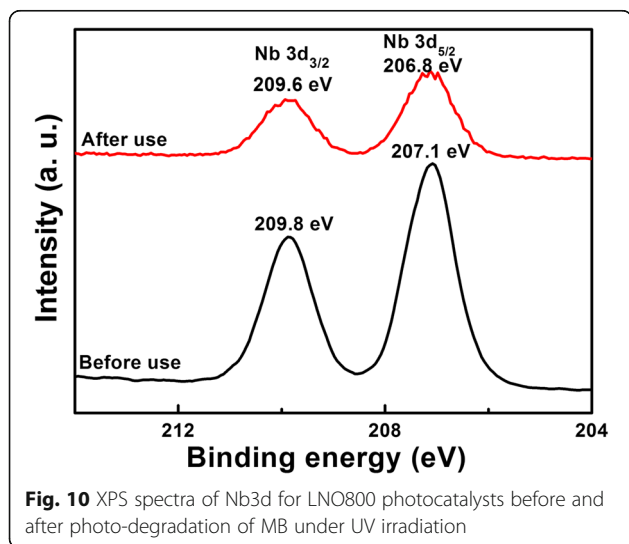
Conclusions

The hollow structure $LiNb_3O_8$ photocatalysts were prepared by the hydrothermal method assisting sintering process. The particles' aggregation to form hollow structures with obvious cavities can be attributed to the Li element volatilization during calcination process. All the $LiNb_3O_8$ powders show high photocatalytic efficiency of the degradation of MB, especially for LNO700, with only 3 h to completely decompose MB. The photo-degradation of MB follows the pseudo-first-order kinetics, and the obtained first-order rate is 0.97/h. The larger degradation rate of LNO700 can be attributed to its hollow structure which provides a larger specific surface area and more active sites to degrade the MB molecules. The cycling test of photo-degradation and adsorption of MB over LNO700 powder indicates that the hollow structure of the $LiNb_3O_8$ photocatalyst is stable and the $LiNb_3O_8$ photocatalyst is an efficient photocatalyst with good reusability for practical applications, confirmed by the XRD and XPS tests before and after photo-degradation of MB.

Authors' Contributions
HZ carried the main part of the experimental work and the XRD measurements. JQ carried the photocatalytic performance tests. XZ, HL, and LY participated in the preparation of the samples. CH carried the SEM images measurements. HL and JY carried the XPS and PL measurements. All authors read and approved the final manuscript.

Competing Interests
The authors declare that they have no competing interests.

Publisher's Note
Springer Nature remains neutral with regard to jurisdictional claims in published maps and institutional affiliations.

References
1. Fujishima A, Honda K (1972) Electrochemical photolysis of water at a semiconductor electrode. Nature 238:37–38
2. Nico C, Monteiro T, Graça MPF (2016) Niobium oxides and niobates physical properties: review and prospects. Prog Mater Sci 80:1–37
3. Abe R, Shinmei K, Koumura N, Hara K, Ohtani B (2013) Visible-light-induced water splitting based on two-step photoexcitation between dye-sensitized layered niobate and tungsten oxide photocatalysts in the presence of a triiodide/iodide shuttle redox mediator. J Am Chem Soc 135:16872–16884
4. Zhai HF, Li AD, Kong JZ, Li XF, Zhao J et al (2013) Preparation and visible-light photocatalytic properties of $BiNbO_4$ and $BiTaO_4$ by a citrate method. J Solid State Chem 202:6–14
5. Zhai HF, Shang SY, Zheng LY, Li PP, Li HJ et al (2016) Efficient visible-light photocatalytic properties in low-temperature bi-Nb-O system photocatalysts. Nanoscale Res Lett 11:383
6. Zhai HF, Kong JZ, Wang AZ, Li HJ, Zhang TT et al (2015) The polymerization effect on synthesis and visible-light photocatalytic properties of low-temperature β-$BiNbO_4$ using Nb-citrate precursor. Nanoscale Res Lett 10:457
7. Wang X, Yan WB, Zhang LX, Shi LH, Chen HJ et al (2015) Tunable photocatalytic activity of photochromic Fe-Mn-codoped $LiNbO_3$ nanocrystals. Opt Mater Express 5:2240–2245

Zhai *et al. Nanoscale Research Letters* (2017) 12:519

Page 7 of 7

8. Liu JW, Chen G, Li ZH, Zhang ZG (2007) Hydrothermal synthesis and photocatalytic properties of $ATaO_3$ and $ANbO_3$ (a = Na and K). Int J Hydrogen Energ 32:2269–2272

9. Liu JL, Shakir I, Kang DJ (2014) Lithium niobate nanoflakes as electrodes for highly stable electrochemical supercapacitor devices. Mater Lett 119:84–87

10. Xu HH, Shu J, Hu XL, Sun YM, Luo W et al (2013) Electrospun porous $LiNb_3O_8$ nanofibers with enhanced lithium-storage properties. J Mater Chem A 1:15053–15059

11. Jian ZL, Lu X, Fang Z, Lu YS, Zhou J et al (2011) $LiNb_3O_8$ as a novel anode material for lithium-ion batteries. Electrochem Commun 13:1127–1130

12. Liu JL, Shakir I, Kang DJ (2014) Single crystalline $LiNb_3O_8$ nanoflakes for efficient photocatalytic degradation of organic pollutants. RSC Adv 4:4917–4920

13. Sahoo PP, Maggard PA (2013) Crystal chemistry, band engineering, and photocatalytic activity of the $LiNb_3O_8$–$CuNb_3O_8$ solid solution. Inorg Chem 52:4443–4450

14. Zielińska B, Borowiak-Palen E, Kalenzuk RJ (2008) Preparation and characterization of lithium niobate as a novel photocatalyst in hydrogen generation. J Phys Chem Solids 69:236–242

15. Zhai HF, Liu HR, Li HJ, Zheng LY, Hu CJ, Zhang X, Li QL, Yang JE (2017) Hydrothermal-assisted sintering strategy towards porous- and hollow-structured $LiNb_3O_8$ anode material. Nanoscale Res Lett 12:463

16. Liu J, Xue DF (2008) Thermal oxidation strategy towards porous metal oxide hollow architectures. Adv Mater 20:2622–2627

17. Wang Q, Qin ZN, Chen J, Ren BS, Chen QF, Guo YC, Cao XF (2016) Green synthesis of nickel species *in situ* modified hollow microsphere TiO_2 with enhanced photocatalytic activity. Appl Surf Sci 364:1–8

18. Yang ZL, Lu J, Ye WC, Yu CS, Chang YL (2017) Preparation of pt/TiO2 hollow nanofibers with highly visible light photocatalytic activity. Appl Surf Sci 392:472–480

19. Jin M, Lu SY, Ma L, Gan MY (2017) One-step synthesis of in situ reduced metal bi decorated bismuth molybdate hollow microspheres with enhancing photocatalytic activity. Appl Surf Sci 396:438–443

20. Zeng XY, Yang J, Shi LX, Li LJ, Gao MZ (2014) Synthesis of multi-shelled ZnO hollow microspheres and their improved photocatalytic activity. Nanoscale Res Lett 9:468

21. Xu C, Lu X, Dai H (2017) The synthesis of size-adjustable superparamagnetism Fe_3O_4 hollow microspheres. Nanoscale Res Lett 12:234

22. Madhusudan P, Zhang J, Cheng B, Yu J (2015) Fabrication of $CdMoO_4$@CdS core-shell hollow superstructures as high performance visible-light driven photocatalysts. Phys Chem Chem Phys 17:15339–15347

23. Wang W, Xu D, Cheng B, Yu J, Jiang C (2017) Hybrid carbon@TiO_2 hollow spheres with enhanced photocatalytic CO_2 reduction activity. J Mater Chem A 5:5020–5029

24. Al-Ekabi H, Serpone N (1988) Kinetics studies in heterogeneous photocatalysis. I. Photocatalytic degradation of chlorinated phenols in aerated aqueous solutions over titania supported on a glass matrix. J Phys Chem 92:5726–5731

25. Rajabi HR, Farsi M (2016) Study of capping agent effect on the structural, optical and photocatalytic properties of zinc sulfide quantum dots. Mater Sci Semicond Process 48:14–22

26. He Y, Zhang YH, Huang HW, Tian N, Guo YX, Luo Y (2014) A novel bi-based oxybromide Bi_4NbO_8Br: synthesis, characterization and visible-light-active photocatalytic activity. Colloids Surf A Physicochem Eng Asp 462:131–136

27. Shi R, Lin J, Wang YJ, Xu J, Zhu YF (2010) Visible-light photocatalytic degradation of $BiTaO_4$ photocatalyst and mechanism of photocorrosion suppression. J Phys Chem C 114:6472–6477

28. Dunkle SS, Suslick KS (2009) Photodegradation of $BiNbO_4$ powder during photocatalytic reactions. J Phys Chem C 113:10341–10345

29. Zhai HF, Liu HR, Li HJ, Zheng LY, Hu CJ, Wang Z, Qi JJ, Yang JE (2017) The effects of Li/Nb ratio on the preparation and photocatalytic performance of Li-Nb-O compounds. Nanoscale Res Lett 12:496